

# THREE-DIMENSIONAL SIMULATION OF FLOODING WAVES IN A VERTICAL PIPE

M. Tekavčič<sup>1</sup>, B. Končar<sup>1</sup> and I. Kljenak<sup>1</sup>

<sup>1</sup> Reactor Engineering Division, Jožef Stefan Institute,  
Jamova cesta 39, SI-1000 Ljubljana, Slovenia, EU  
matej.tekavcic@ijs.si; bostjan.koncar@ijs.si; ivo.kljenak@ijs.si

## ABSTRACT

The results of a three-dimensional transient simulation of air-water churn flow in a vertical pipe are presented using two-fluid modelling approach with interface sharpening. The two phases are considered incompressible and immiscible with no mass and heat transfer between them. Interphase momentum transfer is modelled with interfacial drag force which is based on the interface area density and the relative velocity between the phases. The Continuum Surface Model is used to model the surface tension. The URANS (Unsteady Reynolds-Averaged Navier Stokes) approach is used to simulate the transient behaviour of the churn flow, while the turbulence for each of the phases is being modelled by the two-equation eddy viscosity model. The simulated system is based on experiments from the literature. The numerical domain represents the region around a porous wall liquid inlet of a 19 mm internal diameter vertical pipe test section. Results using gas Reynolds number of 6000 and upward liquid mass flow rate of 25 g/s are presented. The accuracy of the simulations is evaluated on the measured flooding wave amplitudes and frequencies for the churn flow regime obtained from the literature. In addition, the present results are compared with our previous 2D simulations that used the axisymmetric assumption.

## KEYWORDS

churn flow, flooding waves, two-fluid model, numerical simulation

## 1. INTRODUCTION

Flooding or counter-current flow limitation (CCFL) is one of many complex multiphase flow phenomena, which are of particular interest in safety analyses of the loss-of-coolant accident (LOCA) in pressurized water reactor (PWR). During such an accident, part of the primary coolant water flashes to steam due to depressurization of the primary system. Afterwards, when the reflux condenser mode of cooling is established, the upward flow of steam in the central region of a vertical pipe can limit the downward flow of water film on the pipe wall. Flooding develops when the flow of liquid film reverses and cannot penetrate further into the primary system, which in turn limits the cooling of reactor components. There are several examples of vertical flow where CCFL can occur within the PWR cooling systems [1]: the downcomer annulus and the upper core tie plate of the reactor pressure vessel, the riser section of the inverted U-tubes in steam generators, and the pressurizer surge line.

A detailed understanding of the initiating mechanisms is required to predict the onset of flooding. In safety analyses, empirical correlations are usually used, whose validity is typically limited by the range of corresponding experimental conditions. Improved mechanistic models could overcome the limitations of empirical correlations and extensive amount of work was dedicated to investigate flooding phenomena in

the past. However, there are still no available mechanistic models that would adequately predict the onset of flooding [1].

In the case of vertical counter-current gas-liquid flow, such as vertical pipes, channels, and tube bundles, there are two known mechanisms of flooding [2]: the formation and transportation of large liquid waves (A) and entrainment and carryover of droplets beyond the point of liquid entry (B). In pipes with small diameter ( $D < 50$  mm), the large wave mechanism (A) is dominant, whereas droplet mechanism (B) prevails in pipes with larger diameters [2]. These two mechanisms are associated with the two prominent correlations used to predict flooding [2]. The Wallis type correlation [3] incorporates the dependence of the onset of flooding on the pipe diameter. It describes the wave mechanism (A) relevant to small diameter pipes. The Kutateladze type correlation [4] which characterizes the flooding in larger diameter pipes is connected with the droplet entrainment mechanism (B).

The present paper focuses on numerical simulation of large flooding type liquid waves, which can be observed in the churn flow of gas and liquid in a vertical pipe. The churn flow regime can be considered as a transitional regime between slug and annular flow [5]. Experimental study of Govan et al. [6] showed that the transition to churn flow is governed by the capability of forming flooding-type waves. It is believed that the churn flow mechanisms are closely related to the flooding phenomena in vertical pipes [7].

Barbosa et al. [7] examined the formation and motion of flooding type waves in the churn flow regime of air and water in 32 mm internal diameter pipe and presented a model for wave levitation and motion based on the force balance over a coherent circumferential wave. In the experimental procedure, a low up-flow of air was set in the vertical test section at first. The liquid entered at the desired flow rate through a porous wall inlet and flowed downward as a falling film along the wall. Liquid was removed from the test section via the porous wall outlet further down the pipe. Afterwards, the flow of gas was increased until flooding conditions were achieved. In these conditions, large flooding type waves were observed near the liquid inlet, and were transported beyond in the upper part of the test section where waves disperse into entrained droplets. Employing similar approach, the properties of flooding waves were also investigated by Wang et al. [8] using experimental setup with 19 mm, and subsequently also 34 mm [9], internal diameter vertical pipes. The frequencies and amplitudes of flooding waves were measured via flow visualisation with two high-speed CCD cameras. Obtained data are used to evaluate the results of the present simulation.

One of the first numerical simulations of the churn flow were performed by Da Riva and Del Col [10] They have used the FLUENT code and applied homogenous mixture model with the Volume of Fluid (VOF) [11] interface tracking method. Reported simulation results for air-water flow in 32 mm internal diameter pipe have shown qualitative agreement with the data of Barbosa et al [7]. Inhomogeneous two-fluid modelling approach with interface sharpening, which is better suited for modelling of transitional nature of the churn flow, is used in the present numerical simulation. Simulations of churn flow using the two-fluid modelling approach were performed by the ANSYS CFX code [12] and agree with experimental data [7]. It should be noted that both simulations ([10] and [12]) assume axial symmetry of the flow.

Experimental observations [8] [9] of the gas-liquid churn flow in a vertical cylindrical pipe however show, that the circumferential distribution of liquid in the pipe is in general non-uniform, unlike that in the annular flow. Nevertheless, in order to reduce the required computational effort, simulations of churn flow usually use a two-dimensional axisymmetric simplification of the domain [10] [12]. In order to evaluate the differences, in the present study a three-dimensional simulation was performed based on the same experimental data and modelling assumptions than in a previously performed two-dimensional simulation [13].

## 2. NUMERICAL SIMULATION

A three-dimensional transient simulation of vertical air-water churn flow was performed with the Computational Fluid Dynamics (CFD) program ANSYS CFX 15 [14], using experimental data from Wang et al. [8]. The focus of the simulation was on the occurrence of flooding type waves near the porous wall liquid inlet of the vertical pipe [8].

The two-fluid modelling approach with interface sharpening was used to describe the two-phase flow. Each fluid phase is described by its own set of transport equation with additional inter-phase exchange terms that are used to model the transfer of mass and momentum between the phases. In order to sharpen the interface, i.e. reduce the numerical diffusion of the phase indicator variable (volume fraction), Volume of Fluid (VOF) [11] interface tracking method is used within the two-fluid model equations.

### 2.1. Physical Model

The two phases are considered incompressible and immiscible with no mass and heat transfer between them. In the case of incompressible phases  $k$  with no mass and heat exchange, the continuity equation can be written as

$$\sum_k \nabla \cdot (\alpha_k \mathbf{U}_k) = 0, \quad (1)$$

where  $\alpha_k$  is the volume fraction and  $\mathbf{U}_k$  is the velocity field of the phase  $k$ . The momentum equation in inhomogeneous model solved for each phase  $k$  is

$$\begin{aligned} \frac{\partial}{\partial t} (\alpha_k \rho_k \mathbf{U}_k) + \nabla \cdot (\alpha_k \rho_k \mathbf{U}_k \otimes \mathbf{U}_k) = \\ -\alpha_k \nabla p_k + \nabla \cdot (\alpha_k \mu_k^{\text{eff}} (\nabla \mathbf{U}_k + (\nabla \mathbf{U}_k)^T)) + \alpha_k (\rho_k - \rho_{\text{ref}}) \mathbf{g} + \mathbf{D}_{kp} + \mathbf{S}_{kp}, \end{aligned} \quad (2)$$

where  $p_k$  and  $\rho_k$  are the pressure field and density of the fluid phase  $k$ . Both phases share the same pressure field  $p_k = p$ . A buoyancy model based on density difference is included with the  $r_k (\rho_k - \rho_{\text{ref}}) \mathbf{g}$  term, where the density of air is the reference density  $\rho_{\text{ref}} = 1.184 \text{ kg/m}^3$ . The last two terms in Eq. (2) represent the interphase momentum transfer (drag force)  $\mathbf{D}_{kp}$ , and the surface tension force  $\mathbf{S}_{kp}$ .

The momentum exchange between the phases is described by the interfacial drag force

$$\mathbf{D}_{kp} = C_D \rho_{kp} A_{kp} |\mathbf{U}_p - \mathbf{U}_k| (\mathbf{U}_p - \mathbf{U}_k), \quad (3)$$

where  $\rho_{kp} = \alpha_k \rho_k + \alpha_p \rho_p$  is the average density of the flow and  $A_{kp}$  is the interfacial area density that is calculated from the gradient of the volume fraction

$$A_{kp} = |\nabla \alpha_k|, \quad (4)$$

whose minimum value is clipped by the maximum length scale for area density parameter ( $L_{\text{max}} = 1 \text{ m}$ ), so that the condition  $A_{kp} \geq 1/L_{\text{max}}$  is satisfied. The dimensionless drag coefficient  $C_D$  in Eq. (4) is set to the constant value of 0.44.

Surface tension force is modelled with the Continuum Surface Force model [15], with water set as primary fluid  $k$  and air as secondary fluid  $p$ . A constant surface tension coefficient is set to  $\sigma_{kp} = 0.072$  N/m. The surface tension force  $\mathbf{S}_{kp}$  is calculated as

$$\mathbf{S}_{kp} = \sigma_{kp} \kappa_{kp} \mathbf{n}_{kp} \delta_{kp}, \quad (5)$$

where  $\mathbf{n}_{kp}$  is the normal vector of the interface pointing from the primary fluid to the secondary fluid, and  $\kappa_{kp} = \nabla \cdot \mathbf{n}_{kp}$  is the curvature of the interphase surface. The interface delta function  $\delta_{kp}$  is calculated from the gradient of volume fraction. It is effectively zero away from the interface where the surface tension force is not defined.

The air-water flow is considered as transient and turbulent and is thus modelled with an inhomogeneous unsteady Reynolds Averaged Navier-Stokes (URANS) approach with the effective viscosity  $\mu_k^{\text{eff}}$  in the momentum equation (2). Separate turbulence equations are solved for each phase using the Re-Normalisation Group (RNG)  $k - \varepsilon$  model [16] with scalable wall functions.

## 2.2. Computational Domain and Mesh

The computational domain represents the region near the liquid inlet of the vertical pipe with internal diameter  $D = 19$  mm and length  $L = 120$  mm in the experiment of Wang et al. [8]. ICEM CFD software was used to produce three meshes, one of which is shown in Figure 1.

An O-Grid approach was used to mesh the pipe geometry. In the axial direction, the mesh is composed of two cell size regions. Only the water up-flow rate from the experimental data is considered for the mass flow rate boundary condition at the liquid inlet, and therefore the presence of air-water interfaces which should be resolved is not expected. The cell sizes are therefore larger than those above the liquid inlet. As shown in the table in Figure 1, the cell sizes in axial direction are decreasing with ratio of 1.5 from the gas inlet towards the liquid inlet. In the region above the liquid inlet, constant cell axial sizes are used. Second mesh grading is present in the radial direction along the O-Grid Radial edges shown in red in Figure 1.

First mesh M1, with around  $10^5$  cells, has an axial cell size of 0.6 mm above the liquid inlet. Radial cell size grows from 0.15 mm to 0.30 mm from pipe wall towards the centre. There are 28 azimuthal cells, as shown in Figure 1. To produce the second mesh M2 with around  $2 \cdot 10^5$  cells, the number of azimuthal cells was increased to 12 and the number of radial O-Grid cells to 32, which gives radial cell sizes from 0.15 mm to 0.24 mm. The number of axial cells was increased to produce the third mesh M3 with around  $4 \cdot 10^5$  cells, with axial cell sizes of 0.3 mm above the liquid inlet. Details of edge parameters used to produce all three meshes are given in the table in Figure 1.

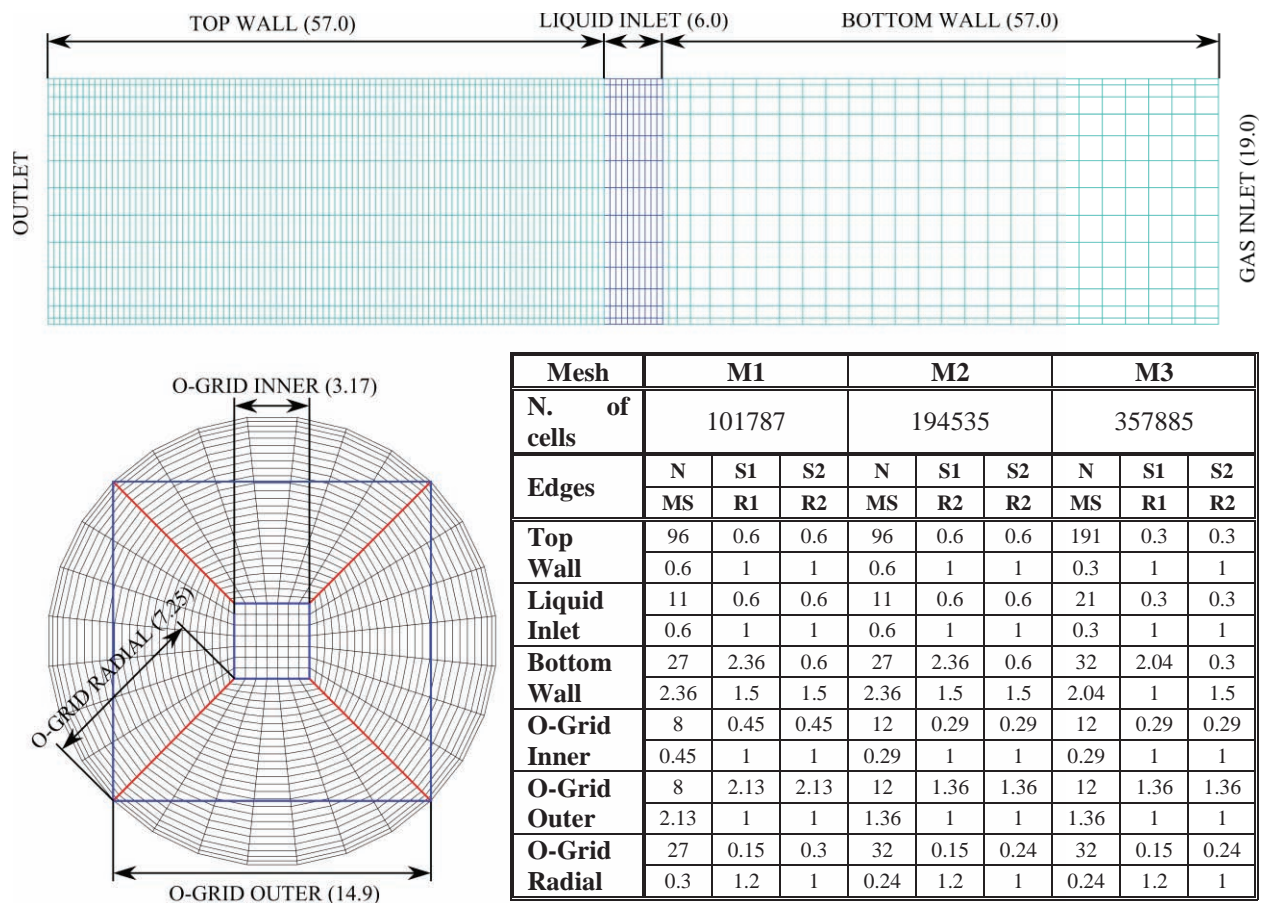


**Figure 1. Side and top view of the geometry and mesh used in the simulation. Lengths of edges in mm are given in parentheses. Parameters used to create three meshes are shown in the table above: N number of nodes, S1/S2 Spacing 1/2 in mm, R1/R2 Ratio 1/2, MS max. spacing in mm**

### 2.3. Boundary Conditions and Numerical Schemes

The turbulent velocity profile at the gas inlet was calculated with a separate steady-state simulation of single phase air flow in longer pipe of length  $4L = 480$  mm with same diameter  $D = 19$  mm as the pipe domain shown in Figure 1. This profile is calculated from the uniform velocity profile of 5 m/s specified at the inlet. A fully developed turbulent flow profile is assumed since  $4L \approx 25D_H > 4.4Re^{1/6}D$ . A turbulence intensity of 10% was set at the gas inlet as suggested in the simulations by Da Riva and Del Col [10].

In the experiment of Wang et al. [8], water was introduced into the pipe through a porous wall section of 18 mm height with 1 mm diameter holes and 2 mm spacing in-between. This porous wall inlet is modelled as a simple uniform surface on the pipe wall with a height of 6 mm as shown in Figure 1, which was already used in previous numerical simulations [10] [12] [13]. A constant liquid mass flow rate of  $\dot{m}_L^0 = 24.98$  g/s is specified at the liquid inlet with turbulence intensity set to 1%. Entry of liquid is delayed in time by 0.1 s in order to further improve the velocity profile of air in the pipe. The following analytic approximation for the Heaviside step function is used for the liquid inlet mass flow rate to smooth the initial transient

$$\dot{m}_L = \dot{m}_L^0 \cdot \left( \frac{1}{2} + \frac{1}{2} \tanh \left( \frac{t-t_0}{\tau} \right) \right), \quad (6)$$

where  $t_0 = 0.1$  s is the delay time and  $\tau = 0.02$  s is the rise time.

The two-phase outlet is modelled as an opening boundary condition with relative pressure set to 0 Pa. The flow direction is calculated by the solver. The zero gradient boundary condition was assumed for turbulence and volume fraction of both fluids at the outlet boundary.

A standard no-slip condition is applied at the pipe wall boundary. Wall adhesion is not considered. In the wall contact model used, the contact area fraction of a fluid phase at the wall is equal to the volume fraction of that phase in the cell adjacent to the wall [14].

All material properties are defined at similar conditions as reported in the experiment [8], that is at the standard atmospheric pressure and 298.25 K (25 °C) and are: the density  $\rho_L = 997$  kg/m<sup>3</sup> and viscosity of water  $\mu_L = 8.899 \cdot 10^{-4}$  kg/(s · m), and the viscosity  $\mu_G = 1.883 \cdot 10^{-5}$  kg/(s · m) of air. The gas Reynolds number calculated from the gas velocity  $U_G = 5$  m/s is  $Re_G = \rho_G U_G D / \mu_G = 6150$ .

Only the net water upflow rate reported in the experiment [8] is considered for the liquid inlet mass flow rate, similarly to the previous simulations [10] [13]. In the experiment, there are two regions of the flow: churn flow regime with flooding waves above the liquid inlet, and counter-current liquid film flow below the liquid inlet. Experiments of Govan et al. [6] showed there are no significant differences in the pressure gradient and liquid holdup above the liquid inlet, when comparing the cases with or without the liquid film flowing below the liquid inlet. Therefore, the aforementioned approach is assumed to be sufficient, since we are interested in the churn flow region above the liquid inlet. The presence of a thin liquid film below the liquid inlet was undesirable in the simulation due to numerical limitations.

A transient simulation with constant time step of  $10^{-2}$ ,  $10^{-3}$  and  $10^{-4}$  seconds was performed on all three meshes. A first-order backward Euler scheme for transient time stepping, first-order upwind scheme for advection, and first-order turbulence numerics were used. A conservation target of 1 % and convergence criteria with RMS Residual Target of  $10^{-4}$  were set, with 2 to 10 internal loops allowed for each time step. Presently, we are unable to obtain converged solutions using more accurate higher order schemes for all three meshes and all three time step sizes. The solver was run in parallel on 10 to 20 processors, depending on the mesh size.

### 3. RESULTS AND DISCUSSION

The occurrence and evolution of flooding waves in the churn flow regime is observed in the simulation. Calculated results for the full flow field are recorded in 10 ms intervals. Additionally, volume fraction and pressure fields are sampled at 1 ms intervals, when  $10^{-3}$  and  $10^{-4}$  s time step sizes are used. Time step and mesh size sensitivity study was performed. Calculated flooding wave amplitudes and frequency are compared with experimental observations from the literature [8]. Results of the present three-dimensional simulation are compared with our previous two-dimensional simulation [13] which use an axisymmetric wedge type mesh of  $800 \times 64$  cells with a size of  $15 \cdot 10^{-5}$  m. This is roughly half size of the M3 cell size presented on Figure 1. Variable time step based on the mean Courant number of 10 and minimum value of  $10^{-4}$  s and maximum value of  $10^{-3}$  s is used for the two-dimensional simulations. In the two-dimensional simulation [8], four cases with increasing inlet gas velocity from 5 to 8 m/s at approximately constant liquid mass flow rate are studied. In such conditions, the flow is approaching the transition from churn to annular flow with increasing gas velocity. Therefore we may assume that the most non-homogeneous circumferential liquid distribution is obtained at the lowest gas velocity of 5 m/s used in the two-dimensional simulation. Only this case is examined in the present simulation.

Figure 2 shows visualisation of the flow in the upper half of the pipe domain calculated with mesh M3 and time step size of  $10^{-4}$  s. Contours of water volume fraction are shown on the vertical cross-section in the middle of the pipe. Visualisation of water surface using contour surface  $\alpha_L = 0.8$  as viewed from the top of the pipe is shown, where colours represent z axis coordinate on such contour surface. The grey shaded surfaces and two vertical lines represent the region between the minimum and maximum wave amplitude reported in the experiment [8]. In this example, the developing coherent wave reaches critical amplitude at around 0.820 s and moves up along the pipe until it reaches the maximum amplitude at approximately 0.838 s and is disintegrated in entrained droplets as can be seen at subsequent times. The liquid exits the domain mainly in the form of liquid film and droplets. Numerous disturbance waves that are of smaller amplitudes or circumferentially incoherent can be observed in the liquid film along the wall.

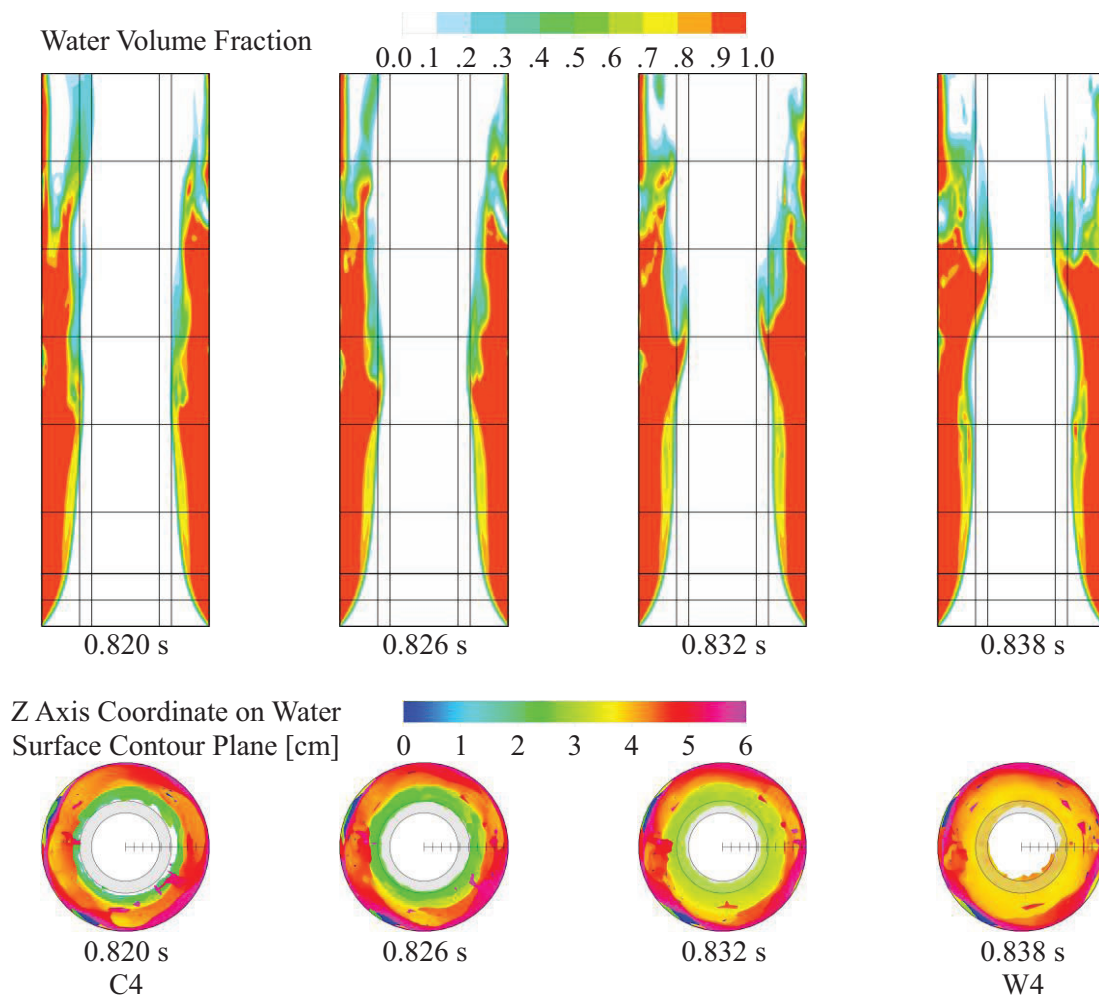


**Figure 2. Transition from critical to maximum amplitude for a selected wave.**  
**Top:** The calculated volume fraction of water in the middle cross section of the pipe (the plane  $y = 0$ ) above the liquid inlet. **Bottom:** Visualisation of water surface using contour surface  $\alpha_L = 0.8$  viewed from the top of the pipe. Colours represent z axis coordinate on such contour surface. Grey shaded area represents the region between the critical and maximum amplitude reported in the experiment [8]. Labels C1 to W4 refer to labels in pressure gradient chart shown in Figure 5. Results were obtained using the mesh M3 and time step of  $10^{-3}$  s.

### 3.1. Mesh and Time Step Sensitivity of Water Volume Fraction

Volume averaged volume fraction of water in the domain is calculated as

$$\langle \alpha_L \rangle_V(t) = \frac{1}{V} \int_V \alpha_L(x, y, z, t) dV, \quad (7)$$

where  $V$  is the volume of the simulated pipe section (see Figure 1). Results are shown on Figure 3 for the three meshes M1, M2 and M3 defined on Figure 1 and three time step sizes of  $10^{-2}$ ,  $10^{-3}$  and  $10^{-4}$  s. In addition, values obtained using our previous two-dimensional simulations [13] are shown in Figure 3 for comparison.

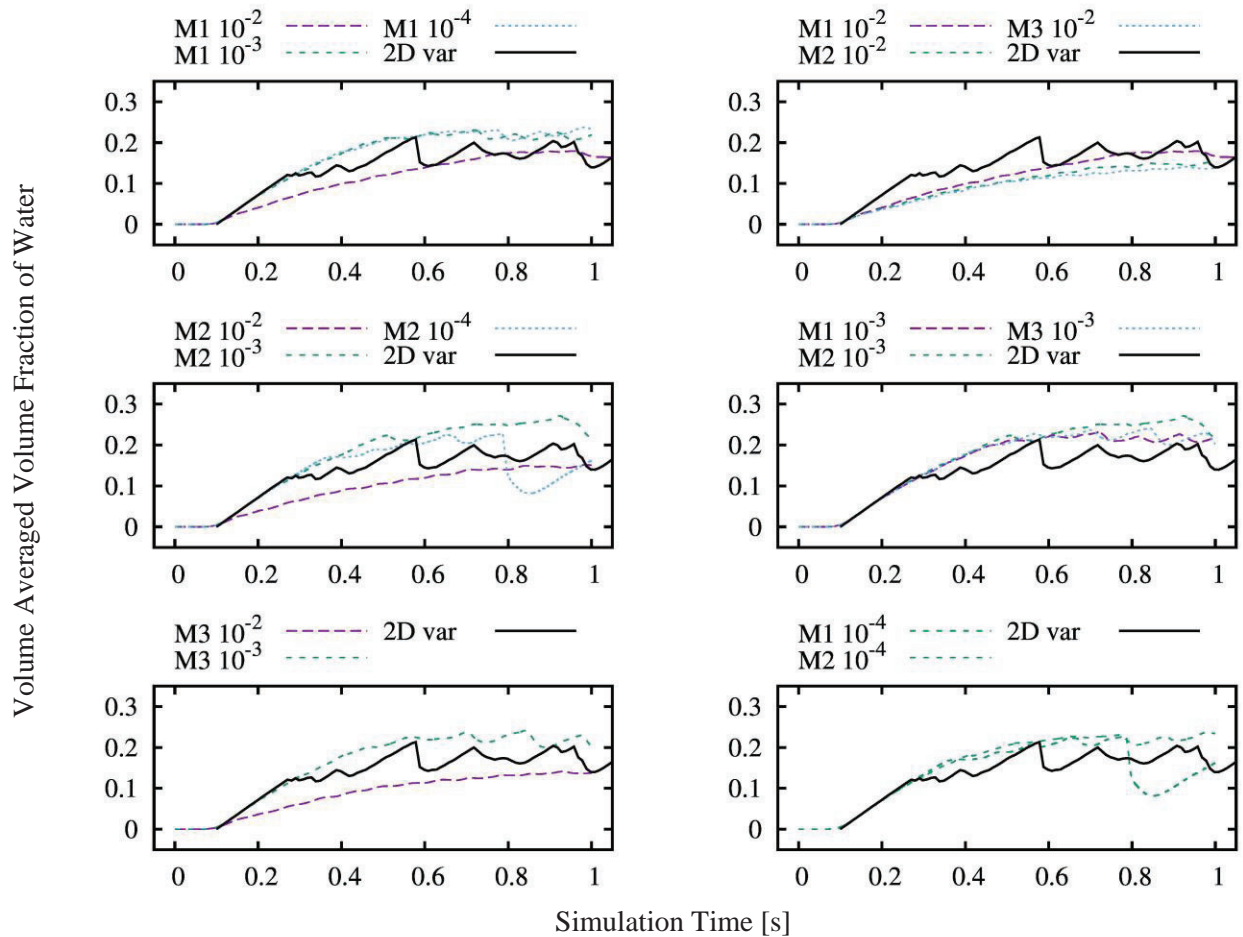


**Figure 3.** Calculated volume averaged water volume fraction (see Eq. (7)) using three different meshes M1, M2 and M3 as defined on Figure 1, and three different time step sizes of  $10^{-2}$ ,  $10^{-3}$  and  $10^{-4}$  s. Values calculated using our previous 2D simulation are shown for comparison.

The results using the time step size of  $10^{-2}$  s on any mesh are significantly different from the results using smaller time step sizes of  $10^{-3}$ ,  $10^{-4}$  s, and variable time step size in 2D calculation. At present, we are unable to explain this discrepancy. It seems that the results are far more sensitive to the time step

size than to the mesh resolution. Namely, for smaller time step sizes than  $10^{-2}$  s, the results using different meshes M1, M2 and M3 are comparable within the 20 % uncertainty band, with the exception of mesh M2 with a  $10^{-4}$  s time step, where the solution deviates significantly at  $\sim 0.8$  s of simulation time. One can observe, at certain time in the simulation (i.e. around 0.4 s) the results start to diverge. This is after the formation of the first few waves, when the simulated flow is assumed to be chaotic. Area averaged volume fraction of water over a pipe cross section  $A$  at height  $z$  is calculated as

$$\langle \alpha_L \rangle_A(z, t) = \frac{1}{A} \int_A \alpha_L(x, y, z, t) dA, \quad (8)$$

and is shown on Figure 4. Height  $z$  is measured from the middle of the vertical pipe domain.

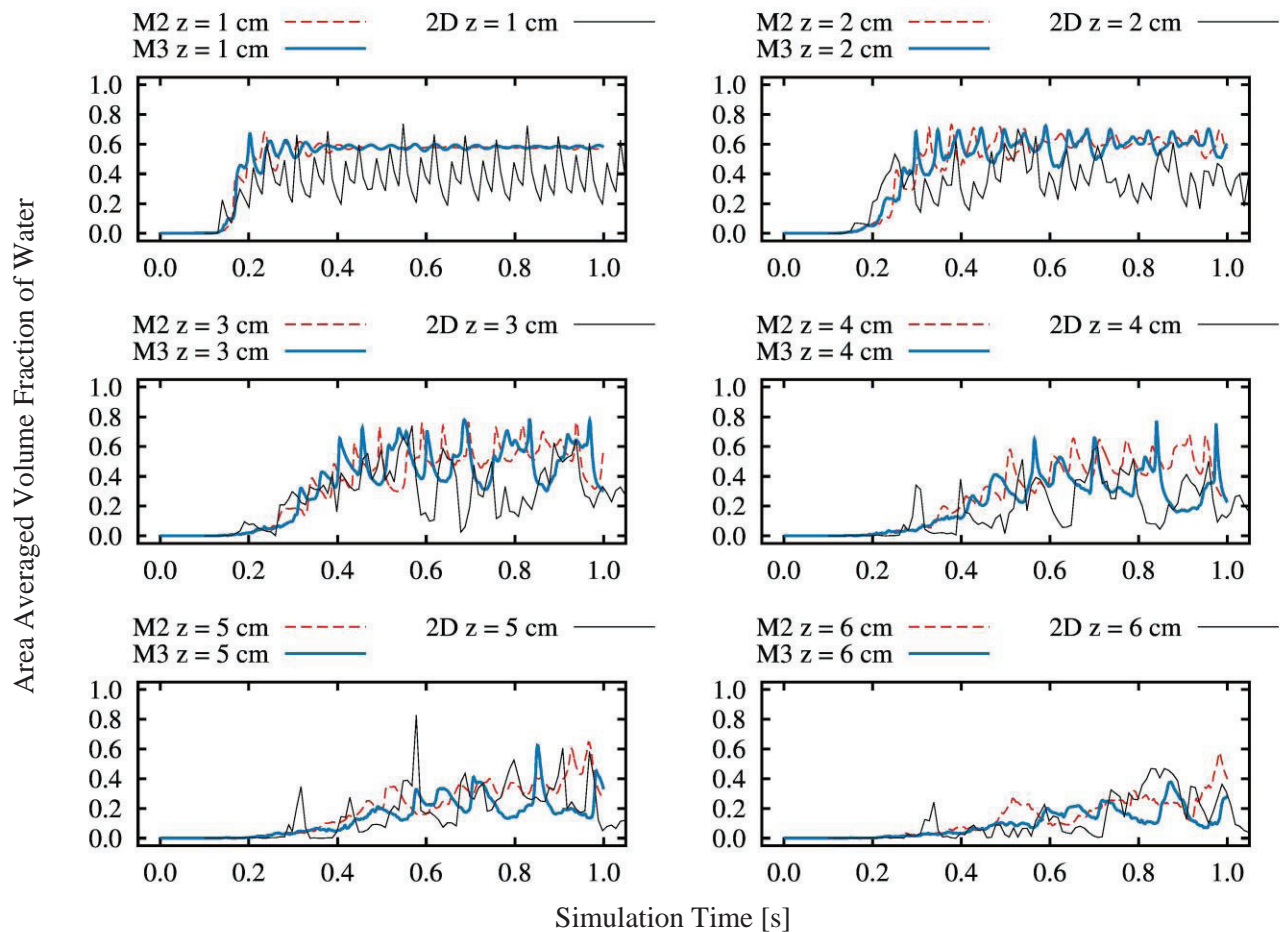


**Figure 4. Calculated area averaged water volume fraction at different heights  $z$  (see Eq. (8)) using different meshes M2 and M3 and time step size of  $10^{-3}$ . Values calculated using our previous 2D simulation are shown for comparison.**

As can be seen on Figure 4, the three-dimensional simulations predict smaller amplitudes of liquid film oscillations when compared to the two dimensional simulation. The difference is more prominent near the liquid inlet and decreases further up towards the end of the pipe ( $z \geq 5$  cm), as shown in Figure 4.

After the initial transient, a quasi-periodic flow can be assumed in the pipe after approximately 0.6 s of the simulation, regarding the results obtained with meshes M1, M3 and two-dimensional calculation. However, such assumption cannot be justified from the results acquired with mesh M2.

### 3.2. Amplitude and Frequency of Flooding Waves

In order to identify large flooding type liquid waves, volume averaged dimensionless pressure gradient is calculated as

$$\frac{dp^*}{dz}(t) = \frac{1}{V} \int_V \frac{dp(x,y,z,t) - \rho_G g}{(\rho_L - \rho_G)g} dV, \quad (9)$$

and is shown on Figure 5. The calculated results for three meshes M1, M2 and M3 using the time step size of  $10^{-3}$  are compared with values obtained with the two-dimensional simulation [13].

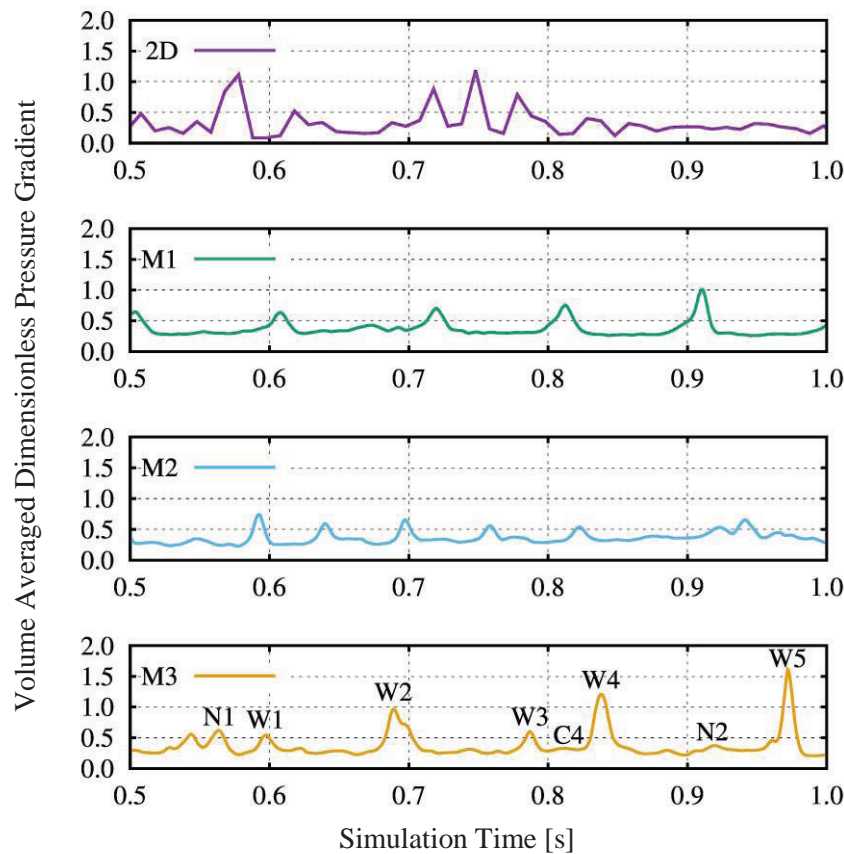


**Figure 5. Calculated dimensionless pressure gradient (see Eq. (9)) using three different meshes M1, M2 and M3 and time step size of  $10^{-3}$ . Values calculated using our previous 2D simulation are shown for comparison.**

The peaks in pressure gradient are observed when a flooding wave of liquid causes a relatively large reduction in the cross-section area of the gas flow at the crest of the wave. At that point, the form drag on the wave is significantly increased and the whole wave is swept upwards along the pipe. These peaks in

pressure gradient are used to identify large flooding waves in the simulation results for the purpose of determining their frequency and amplitude. In the experiment [8] two amplitudes were defined and measured. The wave grows until it reaches the critical amplitude and is carried upwards by the gas. The wave continues to grow until it reaches the maximum amplitude, at which moment the liquid trailing behind the wave and entrainment of droplets in the gas flow balance the liquid that enters the wave. The transition from critical to the maximum amplitude for a selected wave obtained in the simulation is shown in Figure 2.

In the present study, the calculated maximum amplitudes are quantitatively compared with the experimental data [8]. Calculated maximum amplitudes are the amplitudes of waves at the pressure gradient maxima marked as an example with labels W1 to W5 in the results obtained using mesh M3 shown in Figure 5. Certain peaks, such as the two marked with labels N1 and N2 correspond to waves that were not included in determining the amplitude. The wave at label N1 forms when the flow is not yet fully developed, since there is no developed liquid film present on the pipe wall above the wave. These conditions are shown in Figure 6. The second case marked with label N2 shows a wave whose maximum amplitude is smaller even than the reported critical amplitude in the experiment. The dimensionless pressure gradient matching such a wave is also relatively small (less than 0.5) compared to the waves that are included in the analysis. In other words, only the waves that produce dimensionless pressure gradient peaks greater than the threshold value of 0.5 are included when calculating the wave amplitude and frequency. The cases marked with labels N2 and W1 show the two limiting cases with W1 wave above the threshold and included, and wave N2 excluded from the analysis. The effect of using different threshold value for dimensionless pressure gradient (and consequently counting more waves) can be significant when calculating wave frequency, since the number of counted waves is low, i.e. five at mesh M3 due to the rather short simulation time. Unfortunately, obtaining a larger data sample of e.g. 100 waves is unfeasible at present moment due to computational limitations.

The wave maximum amplitudes are calculated using the following procedure. First, the water surface contour of  $\alpha_L = 0.5$  is calculated, similarly to the one used for visualization of the flow in Figure 2. In two-dimensional simulation, it was convenient to define the maximum wave amplitude as the instantaneous maximum distance of such contour from the pipe wall. In three dimensions, the distance of the water surface from the wall also changes along the circumference of the pipe and we would like to obtain an averaged value to compare it also with two-dimensional simulation. Therefore, the wave amplitude is calculated as

$$A_{\max} = R(1 - \sqrt{\alpha}), \quad (10)$$

where  $\alpha = \tilde{A}/A$  represents the ration between the cross sectional area  $\tilde{A}$  for the gas flow at blocked by the liquid wave and the cross sectional area of the pipe  $A = \pi R^2$  as seen from the top of the pipe which is shown in visualization in Figure 2 and 7. In other words, an effective circular cross section for the gas flow is calculated, as if the liquid distribution would be uniform over the pipe circumference. The calculated values for each individual wave are averaged and shown in Table I. The agreement with the wave maximum amplitude measured in the experiment [8] is from -11 % in the worst case using mesh M2 and -2% in the best case using mesh M3. Good agreement was also observed before using the two-dimensional simulation [8]. In this regard, the two-dimensional axisymmetric flow assumption seems reasonable for this particular flow conditions.

The wave frequency is calculated by counting the waves used to determine the amplitude as.

$$f = \frac{N-1}{T_2 - T_1}, \quad (11)$$

where  $N$  is the number of waves identified by peaks in pressure gradient chart in Figure 5 and  $T_2 - T_1$  is the difference between the last and first peak. The calculated results are summarized in in Table I. Unlike the maximum wave amplitude, the discrepancy of calculated values compared to the ones reported in the experiment is considerable. A longer simulation with more counted waves could also significantly affect the accuracy of the result for the wave frequency.

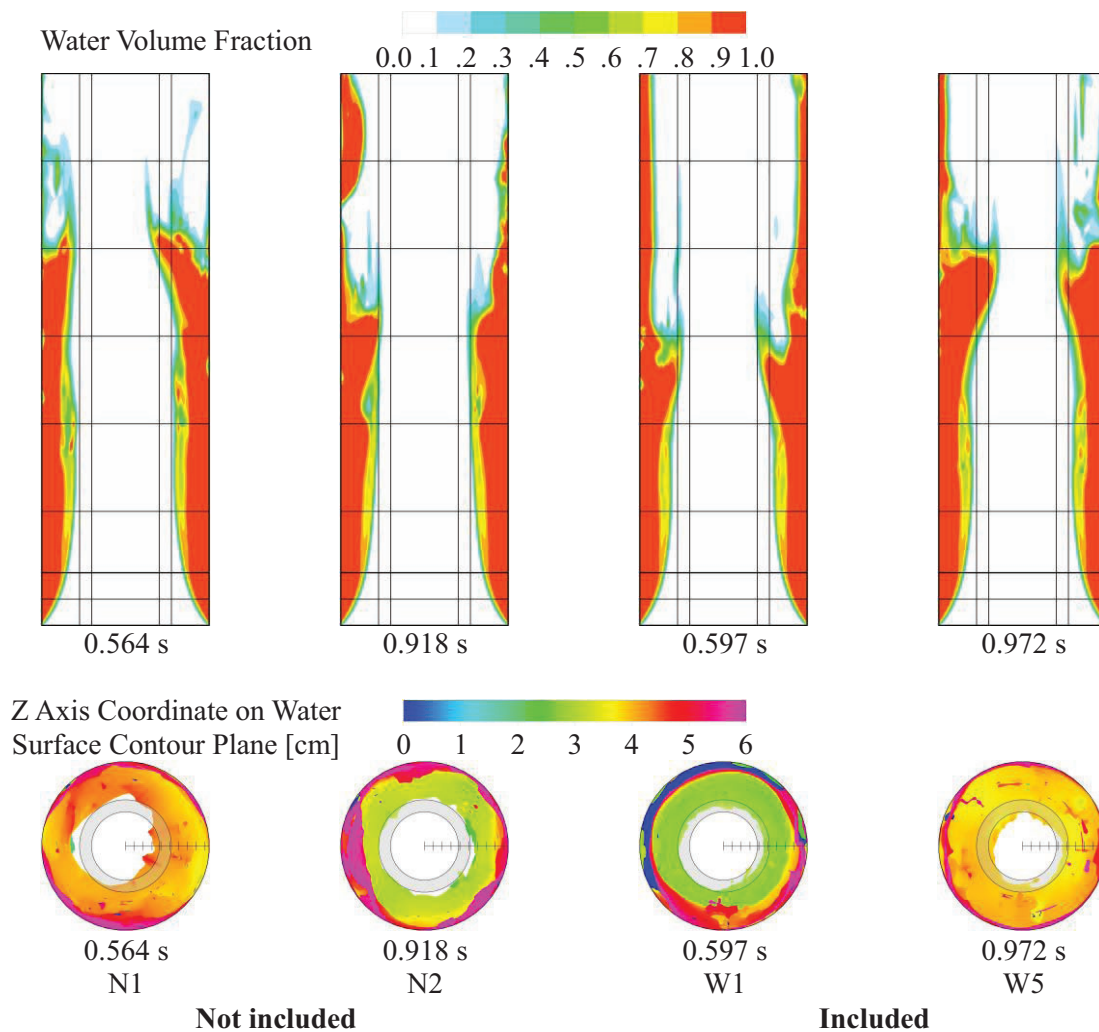


**Figure 6. Examples of two waves not included and two that were included when determining wave amplitudes and frequencies. Refer to text for more detailed explanation. Top: The calculated volume fraction of water in the middle cross section of the pipe (the plane  $y = 0$ ) above the liquid inlet. Bottom: Visualisation of water surface using contour surface  $\alpha_L = 0.8$  viewed from the top of the pipe. Grey shaded area represents the region between the critical and maximum amplitude reported in the experiment [8]. Colours represent  $z$  axis coordinate on such contour surface. Labels N1 to W5 refer to pressure gradient chart shown in Figure 5. Results were obtained using mesh M3 and time step  $10^{-3}$  s.**

It should be noted, that the threshold value for dimensionless pressure gradient of 0.5 used to identify the waves might not be applicable when analyzing results of the previous two-dimensional simulation [13]. Some of the pressure peaks of selected waves in the chart for the two-dimensional case can be attributed to droplets of disintegrated waves, which in turn over-predict the wave amplitude. On the other hand, certain waves that have maximum amplitudes very close to the value reported in the experiment produce a pressure peak with the value less than 0.5 in the two-dimensional case and are thus not included. Nevertheless, adjusting the threshold value is undesirable, since it disables the true comparison of calculated results. Having this in mind, no definite conclusions on the quantitative comparison between the two-dimensional and three-dimensional simulations can be drawn. The spectral analysis of the pressure drop signal in the two dimensional simulation [13] showed the largest peak at the frequency of 16 Hz and the second largest peak at the frequency of 9 Hz, which is closer to the value, obtained by the present method. It was concluded in the paper [12], that the frequency is over predicted by factor of two. Spectral analysis was not performed in the present paper.

**Table I. Calculated wave frequencies and maximum amplitudes using three meshes M1, M2, M3 and time step size of  $10^{-3}$  and the previous two-dimensional simulation. Relative differences of calculated values compared to reported values of 8.79 Hz for frequency and 5.7 mm for the maximum amplitude in the experiment [8] are shown.**

Mesh	N	Frequency [Hz]	Relative Difference	Amplitude [mm]	Relative Difference
2D	5	10.6	21 %	6.0	6.8 %
M1	5	9.83	11.8 %	5.2	-8.7 %
M2	6	14.3	63.0 %	5.0	-11 %
M3	5	10.7	21.3 %	5.5	-2.1 %

#### 4. CONCLUSIONS

A three-dimensional simulation of flooding type waves in the vertical churn flow of air and water was performed. The two-fluid model with the interface sharpening as implemented in the program ANSYS CFX was used. The flow was assumed isothermal. Turbulence was modelled for each phase with inhomogeneous URANS approach. The computational domain represented a region around a test section of a typical experimental setup. The single experimental test case was examined. Mesh and time step sensitivity study showed, that although the obtained results for the amplitude of the waves converge with decreasing mesh discretisation and time step size and agree well with the value reported in the experiment, a longer simulation run is required for improving the accuracy of calculated wave frequency. Qualitatively, the axisymmetric flow assumption seems sound for the particular choice of gas and liquid flow rates in the simulation. No quantitative data on the circumferential uniformity of the flow are available for the examined experiment. Quantitative comparison of wave frequencies is not feasible, since the short simulation time and low number of counted waves have a significant effect on the calculated results when comparing the two-dimensional and three-dimensional simulations.

## ACKNOWLEDGMENTS

This work is partially funded by the Slovenian Research Agency and partially by the European Commission under the 7th EURATOM Framework Program within the NURESAFE Project contract No. 323263.

## REFERENCES

- [1] K. Vierow, "Countercurrent flow limitation experiments and modeling for improved reactor safety," Final Technical Report, Nuclear Engineering Department, TAMU, 2008.
- [2] S. Jayanti, A. Tokarz and G. F. Hewitt, "Theoretical investigation of the diameter effect on flooding in countercurrent flow," *International Journal of Multiphase Flow*, vol. 22, no. 2, pp. 307-234, 1996.
- [3] G. Wallis, „Flooding velocities for air and water in vertical tubes,“ Tech. rep., United Kingdom Atomic Energy Authority. Reactor Group. Atomic Energy Establishment, Winfrith, Dorset, England, 1961.
- [4] D. L. Tien, „A simple analytical model for counter-current flow limiting phenomena with vapor condensation,“ *Letters in Heat and Mass Transfer*, zv. 4, pp. 231-238, 1977.
- [5] G. F. Hewitt, "Churn and Wispy Annular Flow Regimes in Vertical Gas-Liquid Flows," *Energy & Fuels*, vol. 26, no. 7, pp. 4067-4077, 2012.
- [6] A. Govan, G. Hewitt, H. Richter and A. Scott, "Flooding and churn flow in vertical pipes," *International Journal of Multiphase Flow*, vol. 17, no. 1, pp. 27-44, 1991.
- [7] J. R. Barbosa Jr., A. H. Govan and G. F. Hewitt, "Visualisation and modelling studies of churn flow in a vertical pipe," *International Journal of Multiphase Flow*, vol. 27, no. 12, pp. 2105-2127, 2001.
- [8] K. Wang, B. Bai, B. Yang and C. Xie, "Properties of Flooding Waves in Vertical Churn Flow," in *The 14th International Topical Meeting on Nuclear Reactor Thermalhydraulics. Toronto, Canada.*, 2011.
- [9] K. Wang, B. Bai and W. Ma, "Huge wave and drop entrainment mechanism in gas-liquid churn flow," *Chemical Engineering Science*, vol. 104, no. 0, pp. 638-646, 2013.
- [10] E. Da Riva and D. Del Col, "Numerical simulation of churn flow in a vertical pipe," *Chemical Engineering Science*, vol. 64, no. 17, pp. 3753-3765, 2009.
- [11] C. Hirt and B. Nichols, "Volume of fluid (VOF) method for the dynamics of free boundaries," *Journal of Computational Physics*, vol. 39, no. 1, pp. 201-225, 1981.
- [12] M. Tekavčič, B. Končar and I. Kljenak, "Simulation of Counter-Current Gas-Liquid Churn Flow," in *Proceedings of the ASME 2013 Summer Heat Transfer Conference, Minneapolis, MN, USA.*, 2013.
- [13] M. Tekavčič, B. Končar and I. Kljenak, "Simulation of flooding waves in vertical churn flow. CFD4NRS-5," in *Proceedings of CFD4NRS-5, Application of CFD/CMFD Codes to Nuclear Reactor Safety and Design and their Experimental Validation and OECD/NEA & IAEA Workshop, September 9-14 2014, Zurich, Switzerland*, 2014.
- [14] ANSYS, "ANSYS® Academic Research, Release 13.0, Help System, Solver Theory, Multiphase Flow Theory," 2011.
- [15] J. U. Brackbill, D. B. Kothe and C. Zemach, "A Continuum Method for Modeling Surface Tension," *Journal of Computational Physics*, vol. 100, no. 2, pp. 335-354, 1992.
- [16] V. Yakhot and S. Orszag, "Renormalization group analysis of turbulence. I. Basic theory," *Journal of Scientific Computing*, vol. 1, no. 1, pp. 3-51, 1986.